Large eddy simulations of wall jets with coflow for the study of turbulent Prandtl number variations and data-driven modeling

Ali Haghiri[*] and Richard D. Sandberg [ORCID]

Department of Mechanical Engineering University of Melbourne Parkville, Victoria 3010, Australia

There is a continuing effort by turbulence researchers to provide improved turbulent heat flux predictions for Reynolds-averaged Navier-Stokes (RANS) calculations of heat transfer applications. In this paper, data-driven models are developed for the turbulent heat flux prediction in wall jets with coflow using a gene expression programming (GEP)–based machine-learning technique. The training data used as input to the optimization algorithm are obtained by performing highly resolved large eddy simulations (LES) of nine cases covering various flow and geometry conditions. The study examines whether *predictive* RANS-based heat transfer closures can be trained that are robust to these physically very different nine LES cases. The GEP heat flux closures were developed by adopting the gradient-diffusion hypothesis with the optimization target being a nondimensional parameter representing the inverse of a *nonconstant* turbulent Prandtl number (Pr_t), with a functional dependence on the velocity and temperature gradients. First, examination of the turbulent Prandtl number calculated from time-averaged LES data showed a significant deviation from the commonly assumed constant value of 0.9, with a more significant dependence on the lip wall thickness than the blowing ratio. Second, *a posteriori* testing of the developed closures by solving the RANS-based scalar transport equation using as input the LES time-averaged velocity and turbulent viscosity showed a significant improvement in the prediction of adiabatic wall effectiveness not only for the cases they were trained on, but also for the entire matrix of LES cases. Finally, our best-performing model (trained on the thickest lip wall case) was also evaluated in a full RANS context and a significant improvement for the prediction of the adiabatic wall effectiveness was achieved, in particular for the medium and the thin lip thickness cases. The lack of improvement when testing the thickest lip wall case in a full RANS context indicates that for cases with strong vortex shedding the effect of organized unsteadiness on the turbulent flow field is important. In such cases, only modifying the heat flux model without improving the RANS velocity field is not sufficient and other methodologies like deriving a model for the Reynolds stress are necessary. Collectively, the current study demonstrates the ability of the presented model-development framework in creating bespoke models that can provide accurate predictions for a wide range of operating conditions.

DOI: 10.1103/PhysRevFluids.5.064501

I. INTRODUCTION

A wall jet is obtained by injecting a thin jet of fluid tangentially along a solid surface. Along with the jet, there is often a coflow of different velocity and temperature. The interaction of these two flow streams results in different length and timescales (i.e., distinct sets of characteristics and scalings),

---

*haghiri.a@unimelb.edu.au

which has implications for mixing and heat transfer. Wall jets have a wide range of engineering applications such as evaporation enhancement, boundary layer control on high-lift airfoils, cooling of electronic equipment, thin film cooling, and combustion [1–7].

Kacker and Whitelaw [8] experimentally investigated this configuration using a range of fluid and geometry conditions. In particular, they examined how the flow development and mixing are influenced by these factors. Several subsequent numerical studies have used their experimental data for the sake of numerical validation. Holloway *et al.* [9] and Joo and Durbin [10] used unsteady RANS (URANS) and they observed significant differences to the experimental data, particularly the adiabatic wall effectiveness (normalized wall temperature) was poorly predicted.

In wall jet applications, turbulent mixing in the vicinity of walls plays an important role and a correct prediction of this mixing is of crucial importance. The high computational cost of direct numerical simulations, DNS (resolving all flow scales), and large eddy simulations, LES (resolving the majority of flow scales), precludes their use in most practical cases and especially for design iterations in an industrial context. Instead, RANS (modeling all flow scales), due to its acceptable cost, is still widely used as a means of modeling for designers. Nonetheless, RANS poorly predicts the wall temperature because of the inability of RANS closures to reproduce the correct level of turbulent mixing in the near-wall region.

In RANS, the turbulent heat flux is commonly modeled using the gradient diffusion hypothesis (GDH), which dictates that the scalar flux is in the direction of maximum mean temperature gradient (assuming full alignment of these two vectors) and the model acts as a turbulent diffusion term. The diffusivity $\alpha_t = \nu_t/\mathrm{Pr}_t$ is modeled as eddy viscosity ν_t over turbulent Prandtl number Pr_t. The eddy viscosity is commonly modeled using a closure for Reynolds stress and the turbulent Prandtl number is assumed to be constant. $\mathrm{Pr}_t = 0.9$ is widely used in the literature [11–14]. It should be noted that there are alternative approaches to the gradient diffusion hypothesis, such as the generalized gradient diffusion hypothesis (GGDH) [15] that assumes that the turbulent diffusivity is proportional to the Reynolds stresses. This may allow for a better representation of the anisotropic nature of the turbulent diffusivity and also improve the alignment of the turbulent scalar fluxes with the gradients of the mean scalar, particularly in complex three-dimensional flows. Nonetheless, one should be aware that GGDH may not return the correct level of the scalar flux produced in the direction normal to that of the gradient [16]. Also, the heat flux model then depends on the quality of the Reynolds stress model.

Current standard RANS models for turbulent heat flux do not offer the predictive accuracy required. For instance, the assumption of an equilibrium (or quasiequilibrium) between the eddy viscosity and the eddy diffusivity by which the turbulent Prandtl number is assumed to be close to unity may not be valid [17]. Data-driven turbulence modeling has recently shown promise in rectifying some of the model deficiencies and improving RANS predictions via modifying or constructing turbulence models by machine-learning tools [18,19]. In recent years, various data-driven methodologies and machine-learning algorithms [20–22] have been applied to large, high-fidelity data sets to modify the current or developing new turbulence closures. For example, neural networks have been used for secondary flow predictions [23], modeling of anisotropic tensor components of the Reynolds stress (RS) [24], turbulence modeling in subsonic flows around airfoils [25], and predictions of temporally evolving turbulent shear flows [26]. Gaussian processes have modeled corrective terms for channel flows [27] and zonal eddy viscosity models have been proposed by training a decision tree algorithm using incompressible adverse pressure gradient flow test cases [28]. Data-driven calibrations of RANS RS models have also been conducted using experimental data for improved predictions in jet-in-crossflow configurations [29,30].

A novel and quite different data-driven turbulence modeling framework has also been developed [31] based on a form of symbolic regression known as gene expression programming (GEP) [32]. A significant feature of this machine-learning framework is that the result of the optimization is a tangible mathematical expression (instead of just tuning coefficients) which can be easily implemented into any computational fluid dynamics (CFD) solver. In addition, and possibly even more importantly, physical insights can be achieved by inspecting the GEP-constructed models. A

comparison of neural networks and GEP to regress nonlinear stress-strain relationships showed very similar predictive performance, yet the GEP optimization was at a fraction of the cost [33]. Further, GEP was applied to high-pressure [34] and low-pressure [35] turbines and showed significant improvement over the linear model. These studies looked primarily at the stress-strain relationship, yet researchers are also exploring other model components. One group has successfully extracted functional forms for intermittency transport, in order to model bypass transition [36,37].

There are a few machine-learning studies regarding heat-transfer problems. Random forest regression has been applied to model the turbulent thermal diffusivity, for a gradient-diffusion model in the scalar transport of temperature [38] with physical interpretation of data-driven models applied to film cooling flows [39] being highly dependant on distance to the wall and turbulent eddy viscosity. As mentioned, the turbulent wall jet with coflow presents a complex flow field, which makes it difficult to characterize and predict with great accuracy using standard RANS models. In our recent study [40], our GEP machine-learning tool was used to develop heat flux closures with increased prediction accuracy for wall jets with coflow. Although improvements in the prediction of the adiabatic wall effectiveness were observed combining a GEP-trained scalar flux model with a trained RANS Reynolds stress model, the model's robustness was not satisfactory and this simultaneous combination of data-driven heat flux closures with Reynolds stress models in RANS calculations made it difficult to isolate the source of error(s). In fact, the former models' predictive ability to provide more accurate temperature fields was questionable when applied across cases with different flow and geometry conditions. This observation encouraged further investigations on this configuration through training new GEP heat flux models with more robustness and predictive capabilities in the context of RANS.

In this paper, GEP is hence used to develop physics-informed data-driven turbulent heat flux closures based on gradient diffusion hypothesis with improved and robust prediction of RANS temperature fields in wall jets with coflow. The high-fidelity data set as input to the training algorithm comes from performing a matrix of nine highly resolved LES cases using our in-house high-order compressible flow solver HiPSTAR [41], covering a wide range of flow and geometry conditions. To focus on the turbulent heat flux closures only and isolate any other possible sources of error(s), the RANS-based-scalar-transport equation is solved using as input the LES time-averaged velocity field such that only contribution from the heat-flux closures (such as RANS standard eddy diffusivity model and also newly GEP-trained models) is explored. The prediction accuracy and robustness of the GEP models are discussed in detail.

II. FLOW CONFIGURATION AND COMPUTATIONAL SETUP

A. Flow configuration

A schematic of the flow configuration is shown in Fig. 1. At the inlet boundary, a cold wall jet and a plane hot coflow with different speeds are specified, separated by a flat plate with thickness t. This lip thickness controls the strength of the vortex shedding where the two different flows interact and determines the development of the wall jet. In the present study, three different values of the lip thickness normalised with the slot height (s) were considered, along with three different inlet jet velocities. This leads to a total of nine cases featuring different combinations of lip thickness and blowing ratios (BR) and exhibiting different physical phenomena. The inlet mean velocity profiles were adapted from the experimental study of Kacker and Whitelaw [8]. Table I summarizes the simulation parameters.

B. LES setup

The present large eddy simulations (LES) were performed with the in-house multiblock structured compressible Navier–Stokes solver HiPSTAR [42]. After we apply the Favre-filtering
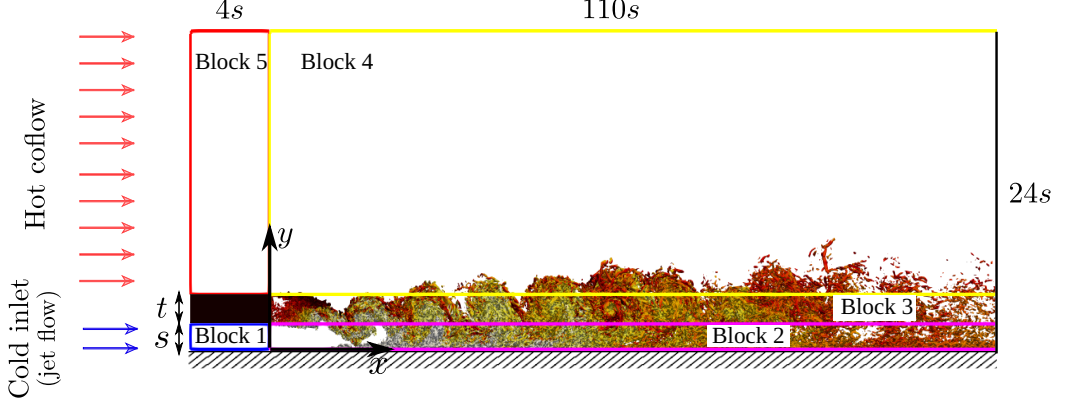
FIG. 1. Computational domain (not to scale) and LES blocks.

operation (defined as $\tilde{f} = \overline{\rho f}/\bar{\rho}$), the filtered Navier-Stokes equations for the conservation of mass, momentum, and total energy are, respectively, as follows:

$$\frac{\partial \bar{\rho}}{\partial t} + \frac{\partial \bar{\rho}\tilde{u}_j}{\partial x_j} = 0, \tag{1}$$

$$\frac{\partial \bar{\rho}\tilde{u}_i}{\partial t} + \frac{\partial \bar{\rho}\tilde{u}_i\tilde{u}_j}{\partial x_j} + \frac{\partial \bar{p}}{\partial x_i} - \frac{\partial \tilde{\sigma}_{ij}}{\partial x_j} = -\frac{\partial \bar{\rho}\tau_{ij}}{\partial x_j}, \tag{2}$$

$$\frac{\partial \bar{\rho}\tilde{E}}{\partial t} + \frac{\partial (\bar{\rho}\tilde{E} + \bar{p})\tilde{u}_j}{\partial x_j} - \frac{\partial \tilde{\sigma}_{ij}\tilde{u}_i}{\partial x_j} + \frac{\partial \tilde{q}_j}{\partial x_j} = -\frac{\partial}{\partial x_j}(\gamma C_V \bar{\rho} Q_j + \frac{1}{2}B_j - D_j). \tag{3}$$

Here ρ is the density, u_j is the velocity component in the x_j direction, p is the pressure, T is the temperature, and $E = e + u_i u_j/2$ is the total energy per unit mass where $e = C_V T$ and C_V are, respectively, the internal energy and the specific heat. The diffusive fluxes are given by

$$\tilde{\sigma}_{ij} = 2\tilde{\mu}\tilde{S}_{ij} - \frac{2}{3}\tilde{\mu}\delta_{ij}\tilde{S}_{kk}, \qquad \tilde{q}_j = -\tilde{k}\frac{\partial \tilde{T}}{\partial x_j}, \tag{4}$$

where $S_{ij} = \frac{1}{2}(\partial u_i/\partial x_j + \partial u_j/\partial x_i)$ is the strain rate tensor, and $\tilde{\mu}$ and $\tilde{k}$ are the viscosity and thermal conductivity corresponding to the filtered temperature $\tilde{T}$.

TABLE I. Simulation parameters.

Case	t/s	BR	Re_{slot}	U_{fs} (m/s)	T_{slot} (K)	T_{fs} (K)
A1	1.14	1.26	$\approx 12\,000$	19.2	273	323
A2	1.14	1.07	$\approx 10\,000$	19.2	273	323
A3	1.14	0.86	$\approx 8\,000$	19.2	273	323
B1	0.63	1.26	$\approx 12\,000$	19.2	273	323
B2	0.63	1.07	$\approx 10\,000$	19.2	273	323
B3	0.63	0.86	$\approx 8\,000$	19.2	273	323
C1	0.126	1.26	$\approx 12\,000$	19.2	273	323
C2	0.126	1.07	$\approx 10\,000$	19.2	273	323
C3	0.126	0.86	$\approx 8\,000$	19.2	273	323

TABLE II. LES grid resolution for each block shown in Fig. 1. Note ($Nx \times Ny \times Nz$) represent the number of grid points in the streamwise, wall-normal, and spanwise directions, respectively.

LES blocks	$t/s = 1.14$	$t/s = 0.63$	$t/s = 0.126$
Block 1	($80 \times 128 \times 66$)	($80 \times 128 \times 130$)	($80 \times 128 \times 130$)
Block 2	($1600 \times 128 \times 66$)	($1600 \times 128 \times 130$)	($1600 \times 128 \times 130$)
Block 3	($1600 \times 128 \times 66$)	($1600 \times 64 \times 130$)	($1600 \times 64 \times 130$)
Block 4	($1600 \times 128 \times 66$)	($1600 \times 128 \times 130$)	($1600 \times 128 \times 130$)
Block 5	($80 \times 128 \times 66$)	($80 \times 128 \times 130$)	($80 \times 128 \times 130$)

The effect of the subgrid scales (SGS) appears on the right-hand side of the governing equations through the SGS stresses τ_{ij}; SGS heat flux Q_j; SGS turbulent diffusion $\partial B_j / \partial x_j$; and SGS viscous diffusion $\partial D_j / \partial x_j$. These quantities are defined as

$$\tau_{ij} = \widetilde{u_i u_j} - \tilde{u}_i \tilde{u}_j, \tag{5}$$

$$Q_j = \widetilde{u_j T} - \tilde{u}_j \tilde{T}, \tag{6}$$

$$B_j = \bar{\rho}(\widetilde{u_j u_k u_k} - \tilde{u}_j \widetilde{u_k u_k}), \tag{7}$$

$$D_j = \overline{\sigma_{ij} u_i} - \tilde{\sigma}_{ij} \tilde{u}_i. \tag{8}$$

The SGS turbulent and viscous diffusion terms [i.e., Eqs. (7) and (8)] are neglected in this study. This is a valid assumption for low to moderate Mach number flows [43]. The wall adapting local eddy viscosity (WALE) model [44] was used for modeling of the subgrid-scale stresses. The WALE model theoretically features the correct near-wall scaling for the subgrid-scale (SGS) eddy viscosity and also is appealing in that no explicit filtering is required and the eddy viscosity is built through only local information [45]. For the density-weighted filtered energy equation, the subgrid-scale heat flux contribution was modeled using subgrid-scale eddy viscosity. It is noteworthy that the ratio of averaged SGS eddy viscosity to molecular viscosity was well below unity, suggesting highly resolved LES. Therefore, for our LES with sufficiently refined grid, the subgrid-scale contribution is negligible as compared to that of the resolved scales.

A fourth-order accurate central differencing scheme was used for the spatial derivatives in the streamwise and wall-normal directions, combined with a spectral method based on the FFTW3 library in the spanwise direction. In addition, skew-symmetric splitting was used to stabilize the convective terms. A five-stage, fourth-order-accurate Runge-Kutta time integrator was used for the temporal discretization.

The LES grid is composed of five blocks as depicted in Fig. 1. The grid resolution for each block is shown in Table II. It should be noted that for the thick-lip cases ($t/s = 1.14$) 32 Fourier modes were used in the spanwise direction, while the other cases (i.e., $t/s = 0.63$ and $t/s = 0.126$) had 64 Fourier modes, corresponding to 66 and 130 collocation points, respectively. In the LES, only mean profiles were prescribed at the inlet and no fluctuations were added. Characteristic boundary conditions were used for the free stream and at the outlet a zonal characteristic boundary condition was employed [46], using 50 streamwise grid points, beginning at $x/s \approx 90$. All walls were set to no-slip boundaries and adiabatic temperature conditions were used. It should be noted that the computational domain was initialized with uniform temperature and velocity fields at $T = 323$ K and $U = 19.2$ m/s, respectively.

The simulations were run using a constant nondimensional time step equal to 6×10^{-4} to satisfy the CFL condition. All cases were initially run for 360 time units, based on slot height and free-stream velocity, to let the initial transient pass. The LES were then continued for another 270 time units in order to collect averaged quantities and statistics. Additional LES were conducted

on different grids and the LES were run for longer and no difference in the results were observed, thus ensuring that the results were grid independent and statistically converged, respectively.

C. RANS-based scalar flux closures

1. The scalar transport equation

Given high computational cost of LES in most practical cases in design context, RANS is still widely used as a means of modeling. However, two sources of errors are associated with RANS calculations: Reynolds stress closures (e.g., Boussinesq approximation) and heat flux models. To isolate the latter, we assume we know velocity field and other inputs to heat flux models accurately (from time-averaged LES in this case). The transport of mean temperature, a passive scalar, for an incompressible flow field is given in the nondimensional form as follows:

$$\frac{\partial \overline{T}}{\partial t} + \overline{u}_i \frac{\partial \overline{T}}{\partial x_i} = \frac{1}{Re\,Pr} \frac{\partial^2 \overline{T}}{\partial x_i \partial x_i} - \frac{\partial \overline{u_i' T'}}{\partial x_i}, \tag{9}$$

where

$$x = \frac{x^*}{L_{ref}}, \; \overline{u}_i = \frac{\overline{u_i^*}}{u_{ref}}, \; t = \frac{t^* \, u_{ref}}{L_{ref}}, \; \overline{T} = \frac{\overline{T^*}}{T_{ref}}. \tag{10}$$

In the above, x and t are the spatial coordinate vector and time, respectively. In addition, u_i is the i component of velocity vector, T is the temperature, Re is the Reynolds number, and Pr is the Prandtl number. It should be also noted that asterisk and overbar represent dimensional and time-averaged variables, respectively. The use of the incompressible framework can be justified as follows. First, the free-stream velocity and maximum jet velocity is well below Mach 0.3. Second, small temperature differences between the jet flow and the free stream imply that buoyancy effects can be neglected from the mean momentum equation. Thus, the energy equation can be decoupled from the momentum equations, allowing for the temperature field to be solved passively.

The heat flux term is usually assumed in the direction of maximum mean temperature gradient and modeled using the gradient diffusion hypothesis as follows [standard eddy diffusivity model (EDM)]:

$$\overline{u_i' T'} = -\alpha_t \frac{\partial \overline{T}}{\partial x_i}, \tag{11}$$

where the diffusivity $\alpha_t = \frac{\nu_t}{Pr_t}$ is modeled as eddy viscosity (ν_t) over turbulent Prandtl number (Pr_t). The eddy viscosity is commonly modeled using a closure for Reynolds stress and the turbulent Prandtl number is assumed to be constant. As mentioned in the introduction, $Pr_t = 0.9$ is widely used in the literature. This simple choice of constant Pr_t indicates that the turbulence acts to isotropically diffuse the heat, which is known not to be the case, except perhaps for simple free shear flows [47]. In the present study, a different approach is chosen and a model for turbulent Prandtl number is obtained as a function of velocity and temperature gradients using the machine-learning framework outlined below.

2. The machine-learning framework

For the present optimization, we choose to use gene expression programming (GEP), a symbolic regression algorithm that returns mathematical equations [32]. We prefer GEP to other tools for several reasons; primarily, we deem the portability and transparency of returning an equation, a valuable characteristic of the process, as it allows for inspection and interpretation of the generated model terms.

In GEP, a close cousin of genetic programming [48], the optimization evolves an initial set of randomly generated candidate solutions ("Create initial populations" block in Fig. 2) by analogy to Darwin's survival-of-the-fittest theory. Each solution is represented as a recursive tree structure.
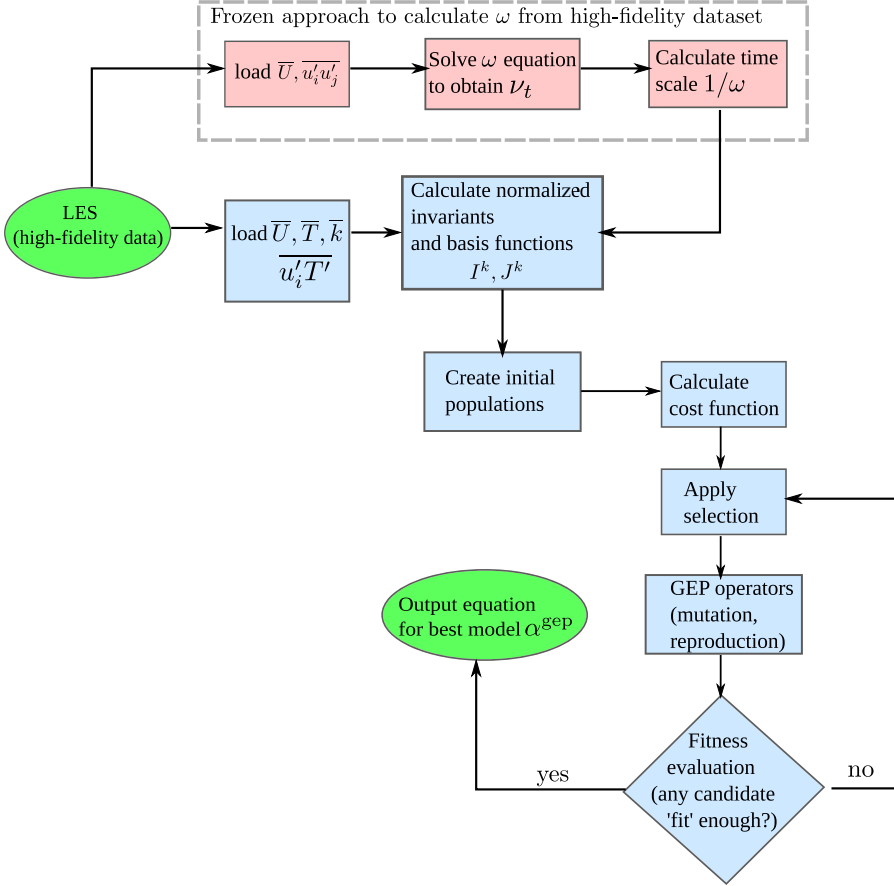
FIG. 2. The GEP heat flux model development flowchart.

Fitness of each individual is evaluated based on a cost function. Selection, or survival of the fittest ("Apply selection" block in Fig. 2) then acts as a filter on the population by weighting the chance of survival in favor of more fit solutions, directing the search away from poorer functional forms. Genetic mutation and reproduction operators then modify these trees ["GEP operators (mutation, reproduction)" block in Fig. 2]. In gene expression programming, mutation is the most important genetic operator. It modifies genomes by changing an element with another (flipping some digits of a string). The accumulation of many small changes over time can create great diversity. Multiple parent reproduction (crossover) is also a genetic operator used to combine the genetic information of two parents to generate new offspring (solutions). Good mutations are retained via the natural-selection process. This causes the population of candidate solutions to iterate toward an optimum solution. For more information, see the work of Koza [48] and Ferreira [32], which are both excellent introductions. The specifics of applying GEP to turbulence models was introduced in detail in Weatheritt and Sandberg [31].

An in-house evolutionary algorithm, which is based on GEP and capable of symbolic regression of scalar, vector, and tensor fields [31], is used. Data-driven closures for turbulent heat flux are developed by adopting the gradient-diffusion hypothesis through minimizing the cost function,

$$\text{CostFun}(\alpha^{\text{gep}}) = \frac{1}{V} \sum_{m \in V} \left\{ \overline{u_i'T'} + \alpha^{\text{gep}} \nu_t \frac{\partial \overline{T}}{\partial x_i} \right\}^{(m)} \left\{ \overline{u_i'T'} + \alpha^{\text{gep}} \nu_t \frac{\partial \overline{T}}{\partial x_i} \right\}^{(m)}, \qquad (12)$$
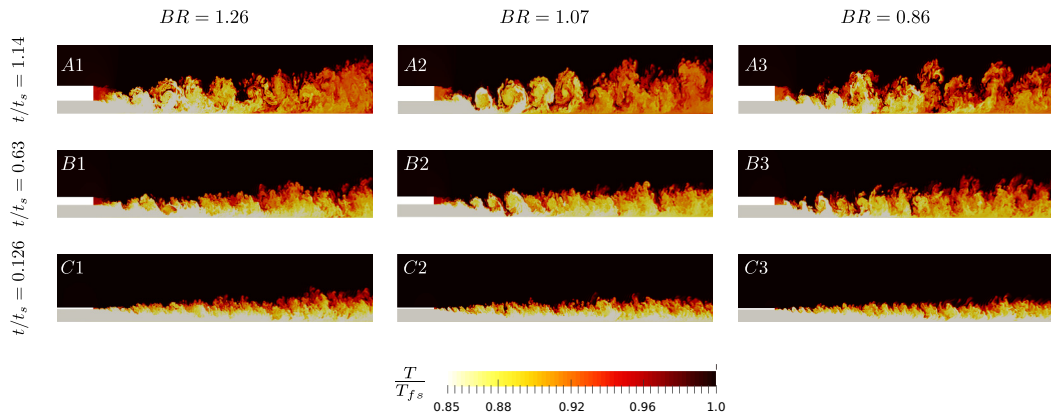
FIG. 3. Instantaneous temperature fields obtained from LES for various lip wall thicknesses (t/s) and blowing ratios (BR). Note that for each plot the streamwise and the wall-normal extents are respectively $x/s = -4 : 30$ and $y/s = 0 : 10$ (not to scale).

which is the mean-square error of Eq. (11), where $\alpha_t = \alpha^{\text{gep}}\nu_t$. Note that V represents the points of our training region. Therefore, the target for optimization is a nondimensional parameter, α^{gep}, which can be considered as the inverse of a *nonconstant* turbulent Prandtl number with a functional dependence on the velocity and temperature gradients,

$$\alpha^{\text{gep}} = f(I^1, I^2, J^1, ..., J^5), \tag{13}$$

where, considering the present statistically two dimensional flows, the function α^{gep} is formed by constructing independent invariants from $s_{ij} = \frac{S_{ij}}{\omega}$, $w_{ij} = \frac{\Omega_{ij}}{\omega}$, and $\vartheta_i = \frac{k^{0.5}}{\beta^*\omega}\frac{\partial \overline{T}}{\partial x_i}$ given as follows (a subset of those given in Ref. [38]):

$$I^1 = s_{ij}s_{ji}, \quad I^2 = w_{ij}w_{ji}, \quad J^1 = \vartheta_i\vartheta_i, \quad J^2 = \vartheta_i s_{ij}\vartheta_j, \quad J^3 = \vartheta_i s_{ij}s_{jk}\vartheta_k,$$
$$J^4 = \vartheta_i w_{ij}w_{jk}\vartheta_k, \quad J^5 = \vartheta_i w_{ij}s_{jk}\vartheta_k. \tag{14}$$

In Eqs. (12) and (13), the turbulence eddy viscosity (ν_t) and the specific turbulence dissipation (ω) are, respectively, needed in our data-driven solutions. As such, ν_t and ω are obtained through a frozen approach in which we hold the true (high-fidelity) velocity and Reynolds stress constant and solve the ω transport equation only, resulting in $\nu_t = \frac{k}{\omega}$, which is consistent with both the high-fidelity database used and the turbulence model equations. Hence, apart from the frozen approach to obtain ν_t, there is no CFD involved in the machine-learning process, which enables us to quickly create heat flux models, typically in less than 10 core minutes.

Figure 2 shows a schematic summarizing the optimization framework in which the standard GEP algorithm is used [32] and tasked with generating functions for α^{gep} out of Eq. (14) by minimizing the cost function defined in Eq. (12). As a result, a data-driven GDH-based closure for the turbulent heat flux is obtained that can be easily used in in any available flow solver. For the current study, we use the open source solver OpenFOAM.

III. RESULTS AND DISCUSSION

A. General flow structure from LES

Figure 3 shows instantaneous temperature fields of the nine LES cases described earlier in Table I. As can be seen, these cases feature different behaviors. Significantly larger vortices are observed, forming behind the lip wall in the thick-lip cases compared with those generated by the
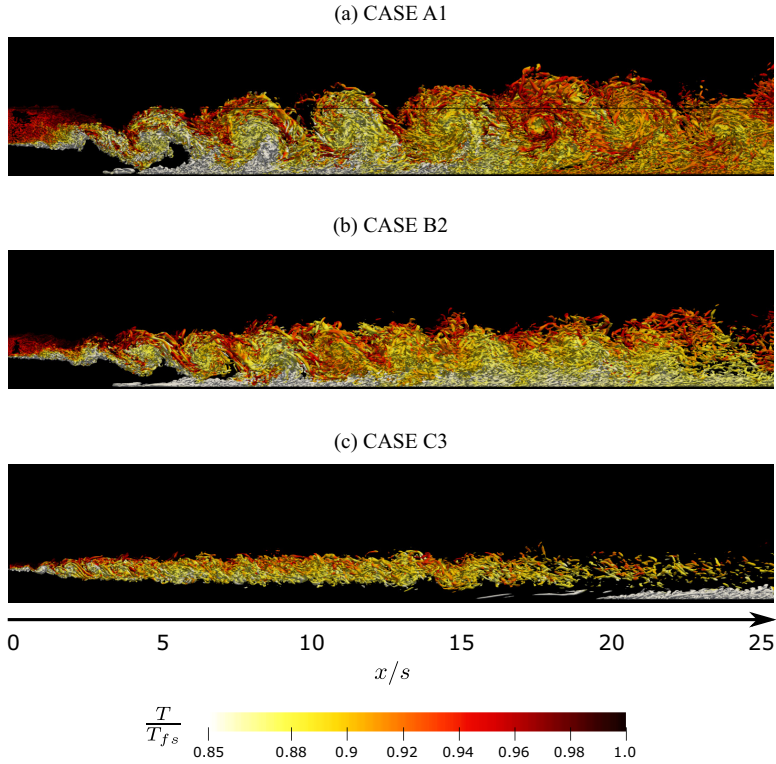
(a) CASE A1

(b) CASE B2

(c) CASE C3

FIG. 4. Instantaneous Q-criterion field (nondimensional isolevel 2) colored with the temperature field obtained from LES cases A1 (a), B2 (b), and C3 (c).

thin-lip ones. This leads to different levels of turbulent mixing of hot and cold fluid seen for the thicker lip cases.

Figure 4 gives a clearer picture of this observation by presenting the instantaneous vortical structures with the Q criterion (the second invariant of the velocity gradient tensor), colored with the temperature field. Three cases, A1, B2, and C3 (diagonal of the cases' matrix) are depicted. It is observed that the larger scale structures generated behind the thick-lip wall carry the hot coflow stream toward the wall much earlier than in the thin-lip case. For the thick-lip case, the first interaction of a large vortical structure with the wall occurs around $x/s = 5$ [Fig. 4(a)], leading to an increase in the wall temperature, whereas for the thin-lip case [Fig. 4(c)], it appears that the wall does not feel the hot stream before $x/s > 25$. This observation will be more quantitatively substantiated by examining the adiabatic wall effectiveness for these cases.

The effect of different lip thicknesses and blowing ratios on the flow dynamics close to the wall is investigated using the time-averaged coefficient of friction (C_f) on the lower wall, as shown in Fig. 5. The coefficient of friction is defined as

$$C_f = \frac{\tau_w}{\frac{1}{2}\rho U_{fs}^2}, \tag{15}$$

where τ_w is the shear stress at the wall and U_{fs} is the freestream velocity. As can be seen, increasing the blowing ratio for a given lip thickness (e.g., cases A3 to A1) does not lead to a significant difference in the near wall behavior of these cases, particularly for $x/s < 5$ (close proximity of the jet exit). For $x/s > 5$, a similar trend is still observed, albeit with the magnitude of C_f being dependent on the blowing ratio. It should be noted that for the thick lip condition (A1)–(A3), there
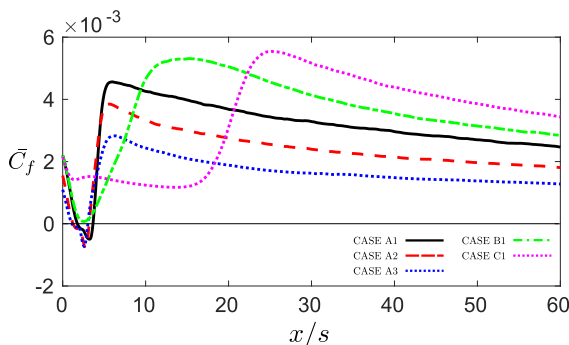
FIG. 5. Mean coefficient of friction along the lower wall.

is a narrow region $2 < x/s < 5$ with a negative value of C_f, indicating the presence of a recirculation zone. Figure 5 also shows that increasing the lip thickness at a given blowing ratio (e.g., cases C1, B1, and A1, respectively) plays an important role in changing the C_f profile so that the wall senses the flow activity above at a significantly earlier distance after the jet exit for the higher blowing ratio (case A1) compared to the lower one (case C1). This can be attributed to the strong shedding of big vortices observed previously in Fig. 4 for case A1.

Figure 6 shows the normalized mean streamwise velocity ($\overline{U}/U_{fs}$) and temperature [$\overline{\theta} = (T - T_{fs})/(T_{slot} - T_{fs})$] at four locations downstream of the jet exit. Of note is that increasing the blowing ratio (BR) at a given lip thickness (t/s) (e.g., cases A3 to A1) results in nearly the same temperature profile, despite the obvious changes in the velocity fields occurring with increasing BR. Looking at the area below the slot height ($y/s < 1$, the region of interest for cooling purposes), increasing t/s at a fixed BR (e.g., cases C1, B1, and A1, respectively) significantly changes both the dynamics and the thermal behavior. This is because of increased mixing of the hot free stream with the cold jet flow due to the large, coherent, vortices generated for thicker lips (see again Fig. 4). This carries heat to the wall for the first few slot heights after the jet exit, which in turn reduces the adiabatic wall effectiveness (i.e., $\overline{\theta}$ at $y = 0$) as can be seen in Figs. 6(ii)(b)–6(ii)(d).

Figure 7 shows profiles of Reynolds stresses (rms values) for a number of streamwise locations. In the near-wall region, the normal stress R_{xx} exhibits larger values compared to the shear stress R_{xy}. However, away from the wall, where the jet interacts with the coflow, these two stress components have comparable magnitudes up to several slot heights downstream of the jet exit. Overall, it is of note that both increasing BR at a given t/s and increasing t/s at a fixed BR result in higher Reynolds stresses, which is more pronounced in regions near to the jet exit. The former is attributed to producing higher momentum by increasing the blowing ratio and the latter is associated with stronger vortex shedding by increasing the lip thickness.

Figure 8 depicts profiles of turbulent heat fluxes (rms values) for the same locations shown previously in Fig. 7. Consistent with the Reynolds stresses, turbulent heat-flux profiles exhibit larger amplitudes close to the jet exit compared to those further downstream. Overall, at $x/s = 3$, streamwise turbulent heat flux features a negative peak in the shear layer near the slot height $y/s = 1$, and a positive peak near the lip thickness. The negative peak highlights that positive streamwise fluctuations associated with fluid motion near the wall bring hot free-stream fluid from above the shear layer down, to mix with the cold jet fluid underneath. Considering the wall-normal turbulent heat flux, only negative peaks in the profiles are observed, indicating that transport across the shear layer and from the wall is driven by positive wall-normal velocity fluctuations and negative temperature fluctuations. It is worth mentioning that increasing BR at a given t/s leads to nearly the same turbulent heat flux profiles, in particular much further downstream. However, increasing t/s at a fixed BR again brings about significant differences, which are more distinct in regions near to the jet exit.
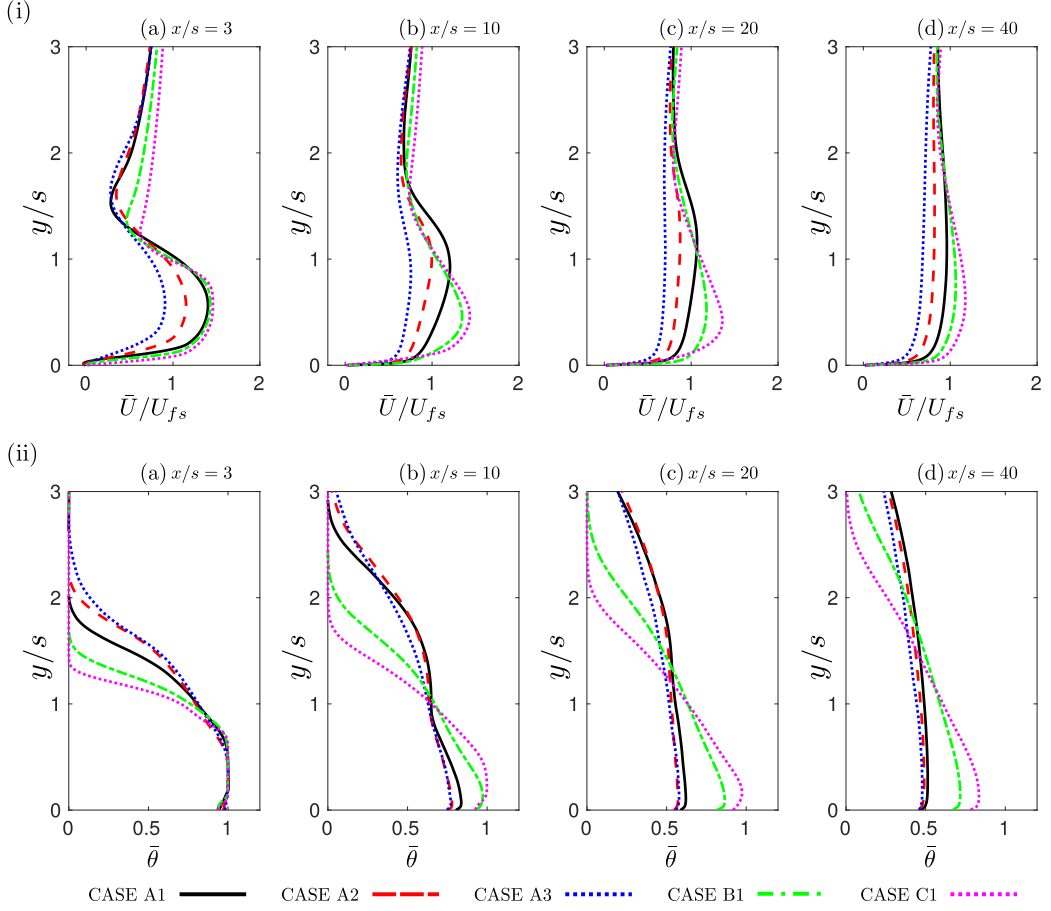
(i)

(ii)

FIG. 6. Normalized mean streamwise velocity (i) and temperature (ii) in a number of locations downstream of the jet exit.

B. Statistics of turbulent Prandtl number (Pr_t) from LES

The turbulent Prandtl number can be calculated from the time-averaged LES data as follows:

$$\mathrm{Pr}_t^{LES} = \frac{\nu_t^{opt}}{\alpha_t^{opt}}, \tag{16}$$

where

$$\nu_t^{opt} = -\frac{1}{2}\frac{S_{ij}a_{ij}}{S_{mn}^2} \quad \text{and} \quad \alpha_t^{opt} = -\frac{\overline{u_i'T'}\dfrac{\partial \overline{T}}{\partial x_i}}{\dfrac{\partial \overline{T}}{\partial x_j}\dfrac{\partial \overline{T}}{\partial x_j}}. \tag{17}$$

Note that ν_t^{opt} is the optimal eddy viscosity and α_t^{opt} is the optimal eddy diffusivity from LES. Further, S_{ij} and a_{ij} are the strain rate tensor and the anisotropy tensor, respectively.

The probability density function (PDF) of the turbulent Prandtl number is shown in Fig. 9 extracted from LES data. The interesting observation is that there is a broad distribution of Pr_t for the LES cases, indicating that a constant turbulent Prandtl number of 0.9 (a commonly used value as discussed in earlier sections) is questionable in general. In fact, the distributions show a
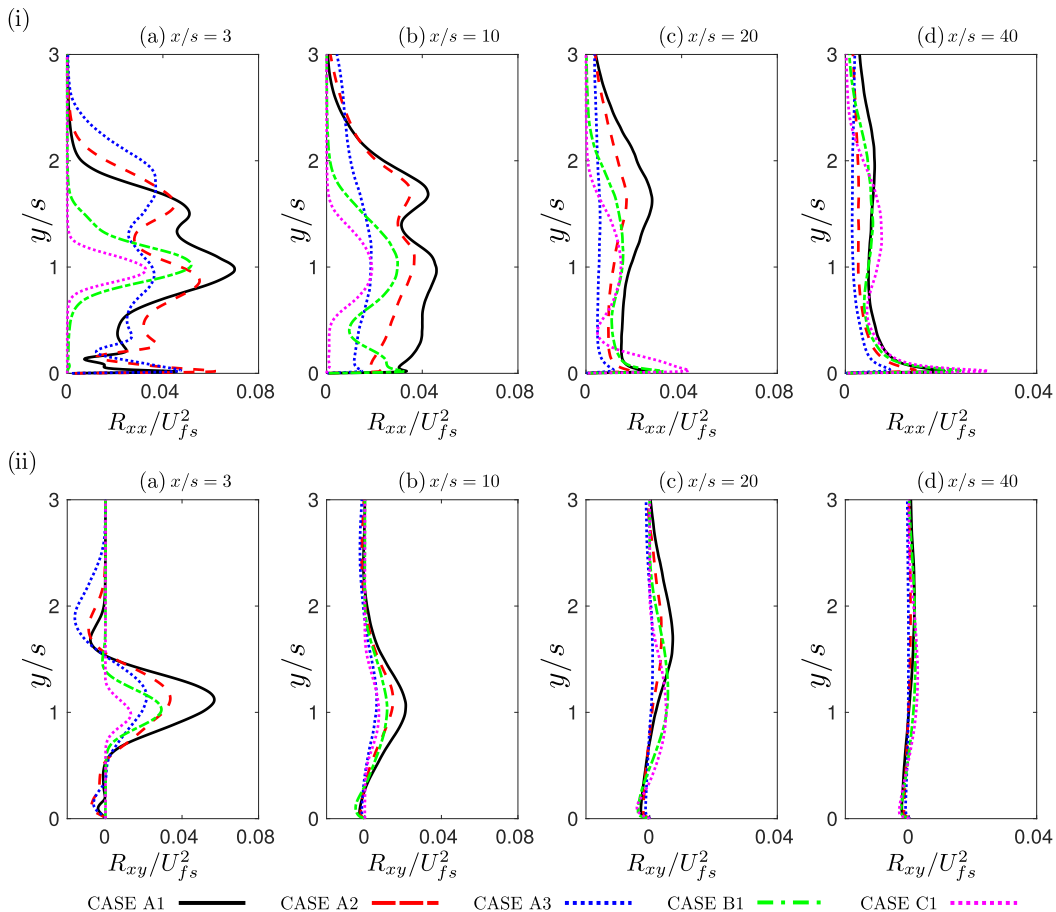
FIG. 7. Reynolds stresses [normal stress R_{xx} (i) and shear stress R_{xy} (ii)] in a number of locations downstream of the jet exit.

strong deviation from the commonly used value toward smaller magnitudes of $\Pr_t$. Furthermore, the $\Pr_t$ for the thickest lip case with different blowing ratios (cases A1–A3) lies predominantly between 0 and 0.6 (having an almost similar probability), with a sudden drop beyond this range; i.e., in no parts of the domain does it get close to $\Pr_t = 0.9$. This indicates that there is no substantial effect of changing the blowing ratio for a given lip thickness on $\Pr_t$, consistent with earlier results presented. However, altering the lip thickness for a given BR (cases A1, B1, C1) results in a significant change of the PDF profiles, which is also consistent with the previous results of the mean and rms quantities. As can be seen, the PDF becomes narrower and its distinct peak moves toward unity as we go for the thinner lip walls. This therefore highlights that for the thinnest lip case the assumption of $Pr_t = 0.9$ is more reasonable. Nonetheless, for cases with strong vortex shedding such as the thickest lip cases studied here, assuming a constant turbulent Prandtl number with value 0.9 is not a good assumption. This assumption will be revisited later in this paper.

The mean turbulent Prandtl numbers (computed from the PDFs) for the LES cases are also presented as a function of lip thickness for different blowing ratios. As can be seen in Fig. 10, for a given blowing ratio, $\Pr_t^{mean}$ decreases significantly with the lip thickness increase. This observation is directly associated with the size of vortices formed behind the lip wall as the smallest $\Pr_t^{mean}$ is seen for the thickest lip case with the biggest shedding vortical structures. Figure 10 also shows that, at a given lip wall thickness, $\Pr_t^{mean}$ increases with increasing the BR, and this variation is
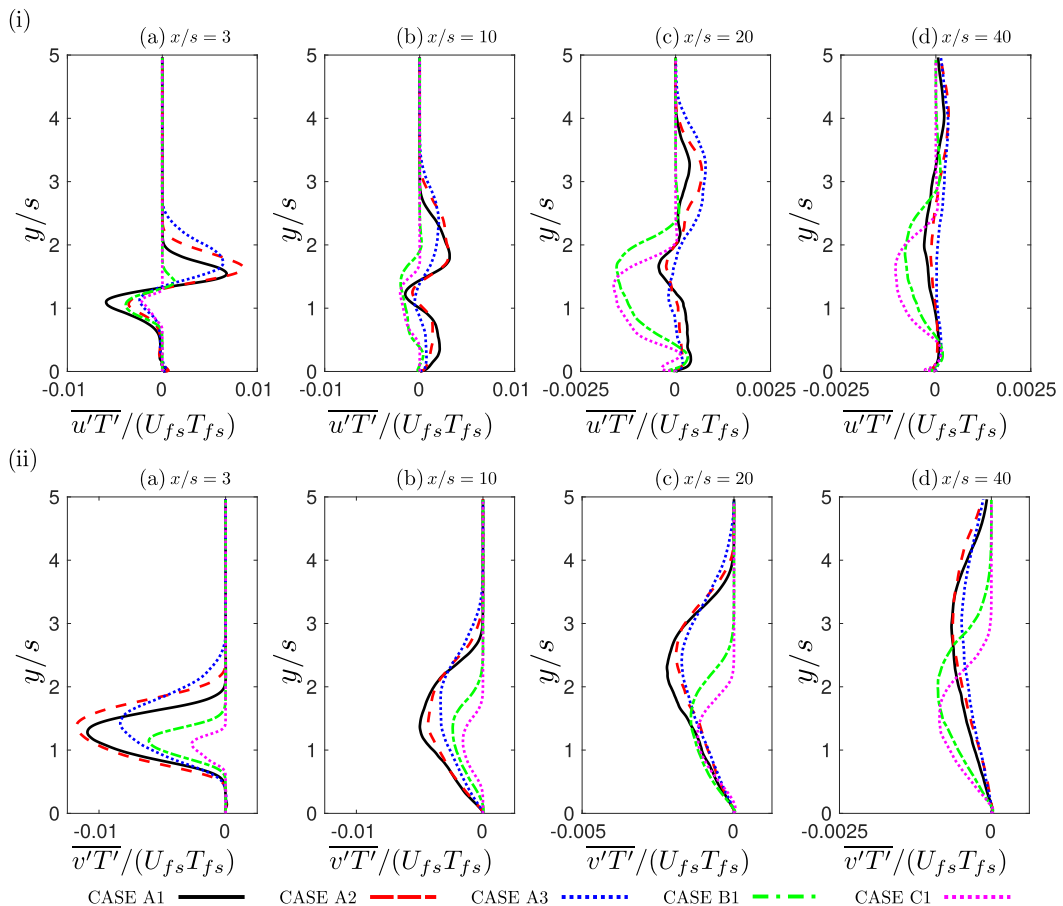
(i)

(ii)

FIG. 8. Turbulent heat fluxes [streamwise component $\overline{u'T'}$ (i) and wall-normal component $\overline{v'T'}$ (ii)] in a number of locations downstream of the jet exit.

more pronounced for bigger t/s. This again highlights the effect of a bigger lip wall thickness on generating complex flow physics that cannot be described simply with a constant Pr_t. Indeed, the common practice in the literature, i.e., considering a constant $\mathrm{Pr}_t = 0.9$, should be revisited. In the current study, we therefore present the use of the high-fidelity data sets for data-driven Pr_t model development.

C. Adiabatic wall effectiveness of standard eddy diffusivity model

Figure 11 shows the adiabatic wall effectiveness [$\eta_{wall} = (T_{wall} - T_{fs})/(T_{slot} - T_{fs})$] for the three LES cases depicted previously in Fig. 4. As can be seen, consistent with the observations in Fig. 4, for the thick- and medium-lip cases, there is a sudden drop in η_{wall} a few slot heights downstream of the jet exit, starting from $x/s > 5$, due to enhanced mixing caused by the large-scale structures. In contrast, for the thin-lip case, the effect of the hot coflow on the wall is negligible up to $x/s \approx 25$ as the cooling flow is not rapidly mixed with the hot free stream flow due to lack of large-scale vortex shedding. These results indicate that the chosen LES cases feature significant differences in their physical behavior and part of the current study is to assess whether heat transfer closures can be trained for steady calculations that are robust to these very disparate cases.
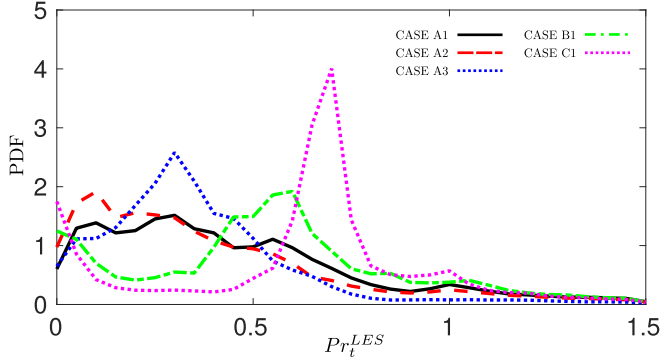
FIG. 9. Probability density function (PDF) of the turbulent Prandtl number Pr_t calculated from time-averaged LES data using Eq. (16).

Figure 11 also compares the adiabatic wall effectiveness between the time-averaged LES results and the results of solving the scalar-transport equation [Eq. (9)] using as input the LES mean velocity field, the frozen eddy viscosity (ν_t) obtained from LES as defined earlier, and the standard EDM with a commonly assumed value of 0.9 for the turbulent Prandtl number (Pr_t). As can be seen, using the scalar-transport calculations with $Pr_t = 0.9$ significantly over predict the adiabatic wall effectiveness for all cases, particularly for the thickest lip wall.

It is therefore understood that the assumption of an equilibrium (or quasiequilibrium) between the eddy viscosity and the eddy diffusivity by which the turbulent Prandtl number is assumed to be close to unity may not be valid. This is the motivation for constructing data-driven models for the turbulent heat flux using the machine-learning framework described earlier.
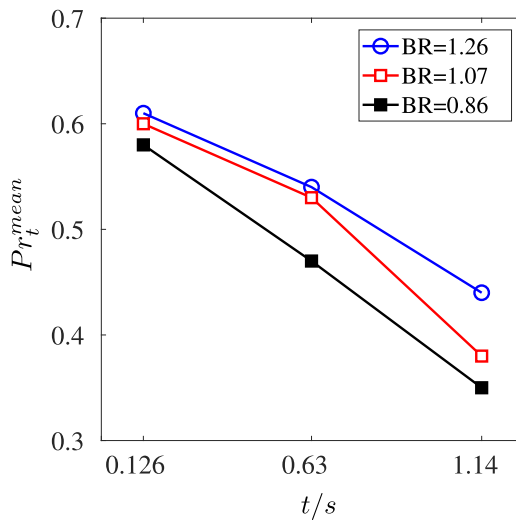

FIG. 10. The *mean* turbulent Prandtl numbers for the LES cases as a function of lip thickness (t/s) for different blowing ratios (BR).
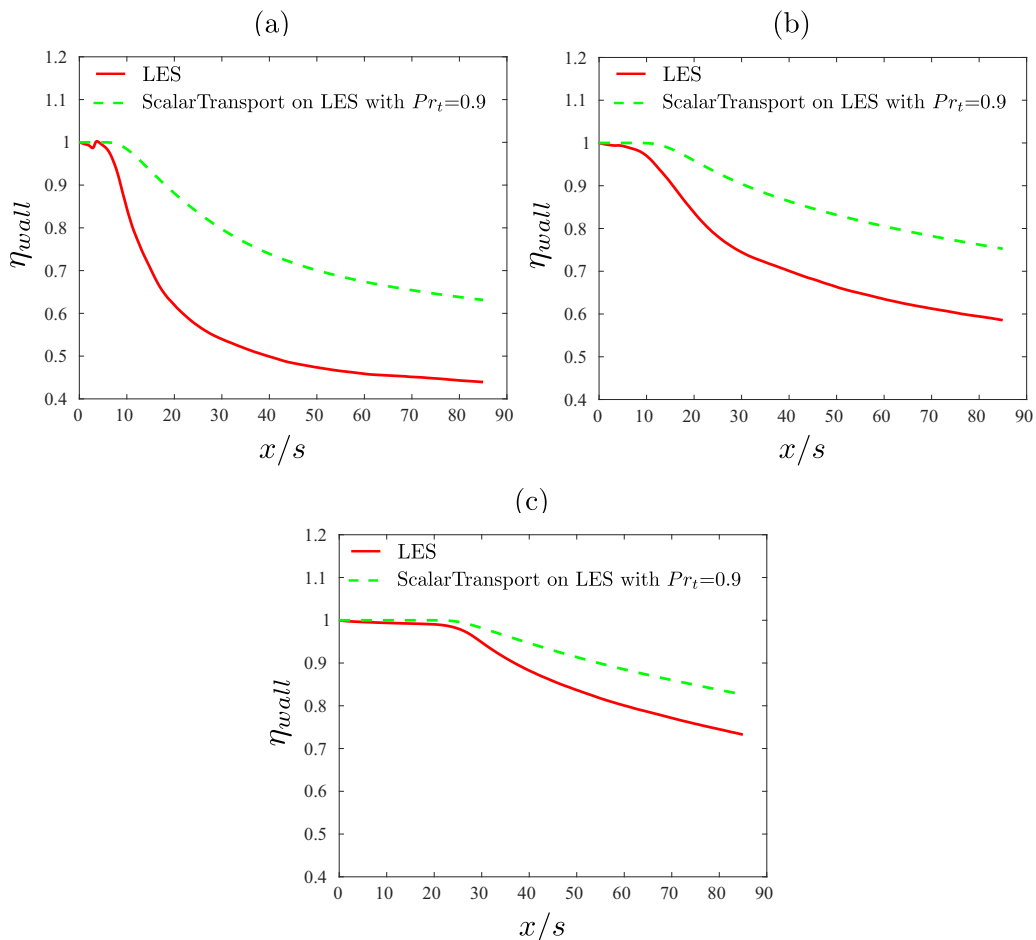
FIG. 11. Comparison of η_{wall} obtained from LES, and the solution of the scalar transport equation [Eq. (9)] as input the time-averaged LES velocity field with the standard eddy diffusivity model with $Pr_t = 0.9$ for cases A1 (a), B2 (b), and C3 (c).

D. Training region and proposed heat flux models

Machine-learning models are generated with the above described framework using the three LES cases discussed in Figs. 4 and 11. The three different models are then tested on all other cases to assess their robustness.

Two training regions are explored for the heat flux modeling as depicted in Fig. 12. In terms of the wall normal extent, these regions encompass $0 \leqslant y/s \leqslant 3$. However, the streamwise locations of the regions differ, with the first region covering $30 \leqslant x/s \leqslant 85$ and the second one extending from $0 \leqslant x/s \leqslant 85$. For the first region, the mechanism of diffusion occurs primarily due to turbulence (stochastic unsteadiness) and not vortex shedding (deterministic unsteadiness). Figure 13 compares the adiabatic wall effectiveness obtained by solving the scalar-transport equation [Eq. (9)] using different heat flux models for case A1, including GEP heat-flux closures developed in these two training regions and also the LES turbulent thermal diffusivity [see Eq. (17) for α_t^{opt}]. In the scalar-transport solution, the GEP models were applied to the whole computational domain after $x/s \geqslant 0$. The case with α_t^{opt} also determines the best possible improvement that we may achieve via our data-driven closures.
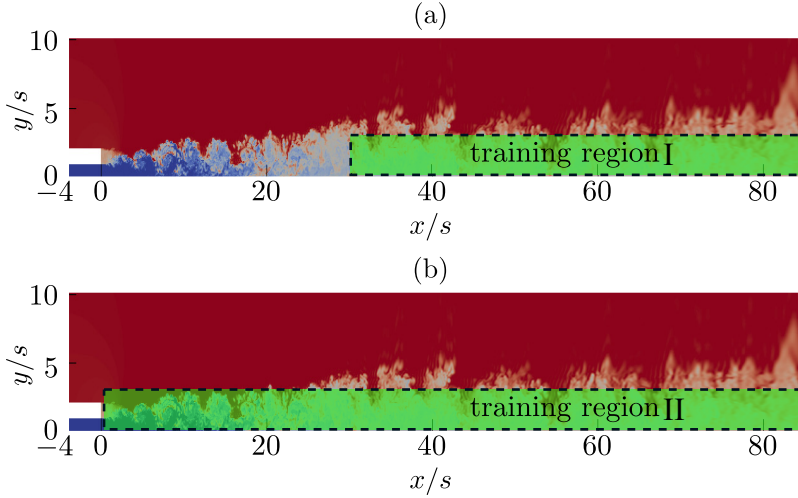
FIG. 12. Training regions for the turbulent heat flux model development.

As can be seen in Fig. 13, significant improvement for the prediction of the adiabatic wall effectiveness is achieved with the machine-learning models. Of note is that the heat flux model developed on the second region results in an underprediction of the adiabatic wall effectiveness (or equivalently overprediction of the turbulent heat flux) further downstream of the jet exit for $x/s > 30$, compared with the best-case scenario of using the scalar transport approach with the LES turbulent heat diffusivity. However, the GEP model constructed using the first training region performs well in this region, with a level of overprediction for $x/s < 30$. Altogether, in what follows in the present study, only the first training region is considered for the model development in which the mechanism of turbulence diffusion (stochastic) does not markedly include the vortex shedding (deterministic) effect. The heat flux closures ($\alpha_t^{mod} = \alpha^{gep} \nu_t$) developed for the three LES datasets using training region I are as follows:
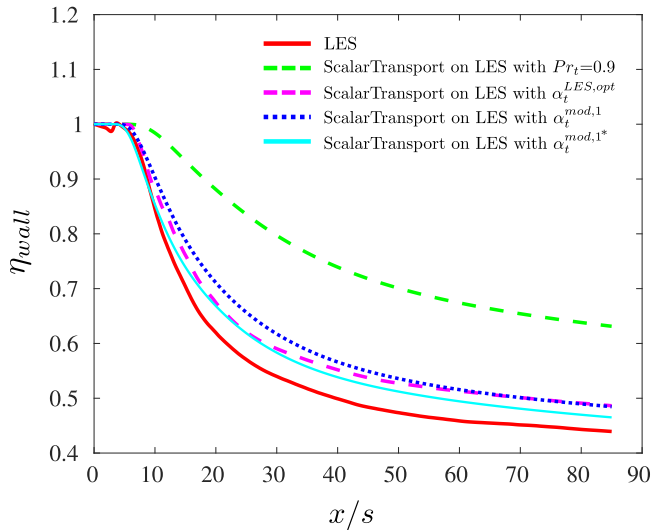

FIG. 13. Comparison of the adiabatic wall effectiveness obtained from different flux models for case A1.

Case A1:

$$\alpha_t^{mod,1} = \{6.806I_2 - 109.407J_1 + 2.0J_2 + 2.368\}\nu_t. \tag{18}$$

Case B2:

$$\alpha_t^{mod,2} = \{0.517I_1 - 0.06I_2 - 20.585J_1 - 11.9J_4 + 2.235\}\nu_t. \tag{19}$$

Case C3:

$$\begin{aligned}
\alpha_t^{mod,3} = \{&3.0I_2 - 2.505I_1 + J_1 - 1.019J_3 + J_4 - 28.0I_1I_2 \\
&+ I_1(43.44I2 - 109.76)(J_1 - I_1 \\
&+ J_2 + J_3) + 1.653\}\nu_t.
\end{aligned} \tag{20}$$

In addition to the three models developed on the three LES cases, another model was created by taking the average of these LES data sets [the scalar invariants (I^k, J^k), the turbulent heat flux ($\overline{u_i'T'}$), and the eddy viscosity (ν_t)] and feeding the averaged fields into the optimization algorithm:

$$\alpha_t^{mod,4} = \{2.247J_1 - 3.15I_2 - 0.0198I_1 - J_2 - 4.0J_3 + 7.247J_4 + 1.995\}\nu_t. \tag{21}$$

It should be noted that since the present GEP optimization is a stochastic, supervised machine-learning approach, by running the framework with a new initial guess, we get a different form of the mathematical expression as the output of the optimization, but with the same performance when tested *a priori* and *a posteriori*.

It is of importance to understand the differences that these models offer in comparison with the EDM with $\Pr_t = 0.9$. Figure 14 shows the turbulent thermal diffusivity α_t calculated from time-averaged LES ($\alpha_t^{LES,opt}$), the EDM with $\Pr_t = 0.9$ (α_t^{EDM}), and the developed GEP closures at two different axial locations. As can be seen, $\alpha_t^{LES,opt}$ is significantly underpredicted by α_t^{EDM}, whereas there is an excellent agreement between α_t^{GEP} and the LES profiles. This indicates that the optimization framework has performed well in developing the heat flux closures, and the GEP models can therefore be evaluated with confidence *a posteriori* in the RANS framework.

Figure 15 shows the PDF of the turbulent Prandtl number along with the contribution from only the constant term in each developed data-driven model [i.e., Eqs. (18), (19), and (20)] illustrated with an arrow. As can be seen, the contribution of the basis functions (i.e., nonconstant terms) to the PDF of $\Pr_t$ becomes significant when the lip wall thickness increases. As such, for the thinnest lip wall case [see Fig. 15(c)] [where the deviation from the contribution of only the constant term in Eq. (20) is not as significant as for the thicker lip wall cases] assuming a constant $\Pr_t = 0.6$ appears to be reasonable; however, the large deviations for bigger lip wall thickness cases highlights the roles played by the basis functions in the models. The latter also indicates the value of including local mean flow behaviors in the model for the turbulent Prandtl number (i.e., providing a nonconstant $\Pr_t$ as function of velocity and temperature gradients).

E. Comparison of modeled and LES adiabatic wall effectiveness

Figure 16 shows the adiabatic wall effectiveness (η_{wall}) of all the nine LES cases calculated using the heat flux models developed earlier. As can be seen, when the model trained on a particular lip thickness is used on the other blowing ratios of that geometry, there is a significant improvement in the η_{wall} prediction, which is consistent across all cases. Further, it is also of importance to examine the adiabatic wall effectiveness profiles when a particular model is used on a different geometry and blowing ratio from how it was developed, e.g., when trained models are applied to cases previously unseen. A significant and consistent improvement in the results is again observed for the thick and medium lip thickness geometries using the data-driven models $\alpha_t^{mod,1}$, $\alpha_t^{mod,2}$, and $\alpha_t^{mod,4}$. However, by applying these models to the thin-lip case, a level of underprediction of the η_{wall} is observed; nonetheless, the profiles have improved considerably compared to those of the EDM with $\Pr_t = 0.9$. There is an overprediction of the η_{wall} when the model trained on the thinnest geometry ($\alpha_t^{mod,3}$)
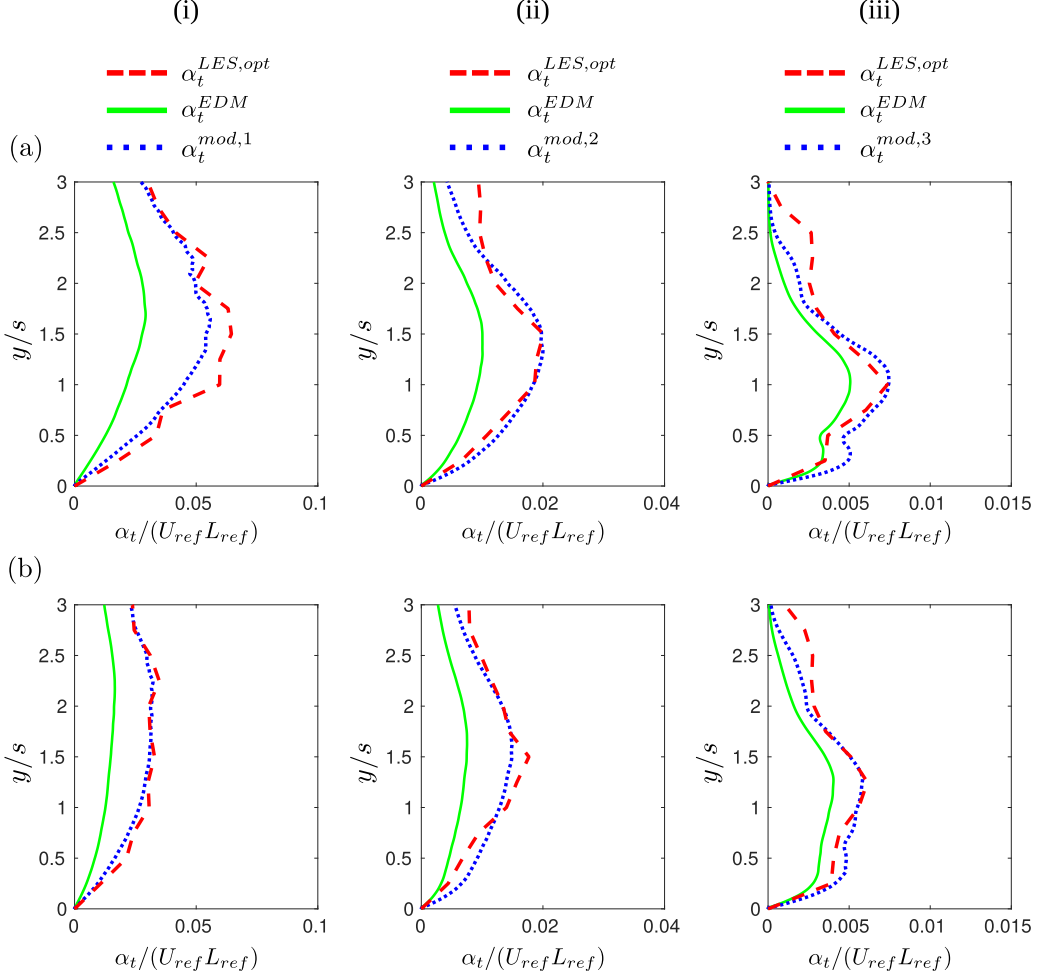
FIG. 14. Turbulent thermal diffusivity α_t calculated from time-averaged LES ($\alpha_t^{LES,opt}$), standard eddy diffusivity model with $Pr_t = 0.9$ (α_t^{EDM}), and the developed GEP closures [i.e., $\alpha_t^{mod,1}$, Eq. (18); $\alpha_t^{mod,2}$, Eq. (19); and $\alpha_t^{mod,3}$, Eq. (20)] for cases A1 (i), B2 (ii), and C3 (iii) at $x/s = 30$ (a) and $x/s = 45$ (b).

is applied to the other geometries, but the η_{wall} profiles are still remarkably improved compared to the $Pr_t = 0.9$ case. This observation can be attributed to the smaller flow structures in the thinnest lip case compared to the thicker lip wall geometries (see Fig. 4 for a clearer picture). In the former, the vortex shedding frequency is higher and does not persist for a long downstream distance, while in the latter the low-frequency vortex shedding is produced by the lip wall that persists for a large distance downstream.

Table III quantifies the percent error reduction in the prediction of the adiabatic wall effectiveness by using the data-driven turbulent heat flux models compared with the EDM with $Pr_t = 0.9$,

$$\left\langle \frac{E_{EDM} - E_{GEP}}{E_{EDM}} \right\rangle 100, \tag{22}$$
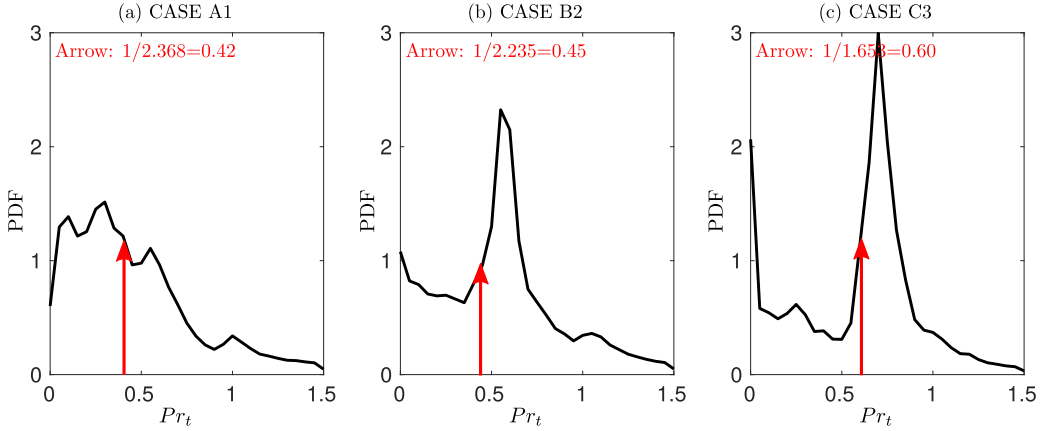
FIG. 15. The PDF of the turbulent Prandtl number along with the contribution from only the constant term in each developed data-driven model [i.e., $\alpha_t^{mod,1}$, Eq. (18); $\alpha_t^{mod,2}$, Eq. (19); and $\alpha_t^{mod,3}$, Eq. (20)] illustrated with arrows.

with

$$E_{model} = \sqrt{\frac{\int_0^{L_x} (\eta_{model} - \eta_{LES})^2 \, dx}{\int_0^{L_x} \eta_{LES}^2 \, dx}}. \tag{23}$$

As can be seen, using the GEP models on the cases on which the training was performed (the highlighted cells in Table III), a significant error reduction between 71 and 93% is obtained. Applying these models to other cases unseen in the model development also leads to a considerable error reduction; in particular, the model ($\alpha_t^{mod,1}$) developed on the thickest lip wall ($t/s = 1.14$)

TABLE III. The percent error reduction in the prediction of the adiabatic wall effectiveness by using the data-driven turbulent heat flux models compared with the standard eddy diffusivity model (EDM) with $\mathrm{Pr}_t = 0.9$.

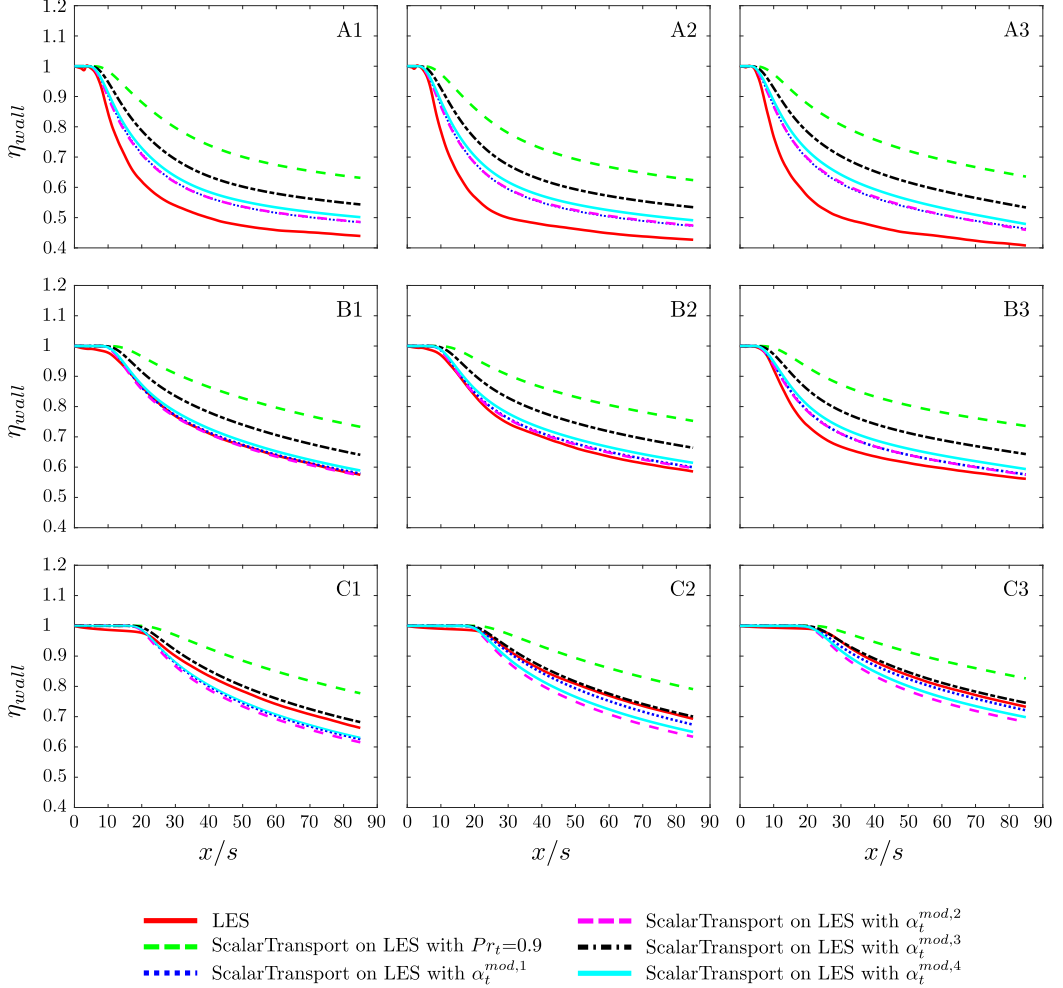|	BR	1.26	1.07	0.86
t/s				
	$\alpha_t^{mod,1}$	**71%**	68%	66%
	$\alpha_t^{mod,2}$	71%	68%	65%
1.14	$\alpha_t^{mod,3}$	41%	39%	36%
	$\alpha_t^{mod,4}$	63%	60%	60%
	$\alpha_t^{mod,1}$	96%	91%	83%
	$\alpha_t^{mod,2}$	96%	**93%**	83%
0.63	$\alpha_t^{mod,3}$	56%	50%	46%
	$\alpha_t^{mod,4}$	90%	81%	73%
	$\alpha_t^{mod,1}$	63%	81%	83%
	$\alpha_t^{mod,2}$	53%	33%	35%
0.126	$\alpha_t^{mod,3}$	80%	88%	**86%**
	$\alpha_t^{mod,4}$	68%	51%	55%

FIG. 16. Comparison of the adiabatic wall effectiveness obtained from different flux models.

case at BR = 1.26 performs well across all the cases with an error reduction of 83–96% for the medium-lip cases ($t/s = 0.63$) and of 63–83% for the thinnest lip geometries ($t/s = 0.126$). It should be noted that, as discussed earlier, the model trained on the thinnest lip wall case (case C3) shows a better improvement in the η_{wall} profiles of this geometry with an error reduction in the range of 80–88%; nevertheless, applying the other models on this geometry still remarkably improves the results. It is also worth noting the model trained by feeding the averaged fields of the three LES cases A1, B2, and C3 to the machine-learning algorithm [i.e., model 4, see Eq. (21)] performs properly across all the cases with an error reduction of 51–90%. Altogether, these results indicate that the heat flux models developed in the present study are predictive models and are able to significantly improve the prediction of the adiabatic wall effectiveness for very different operating conditions.

We previously showed that a model trained in a particular flow and geometry condition can also lead to significant improvement in the prediction of adiabatic wall effectiveness when used for cases unseen in the training procedure. For example, as shown in Table III, the model ($\alpha_t^{mod,1}$) developed on the thickest lip wall ($t/s = 1.14$) case at BR = 1.26 performs well across all the cases with a significant error reduction of 63–96%. This can be regarded as a means of robustness for the models
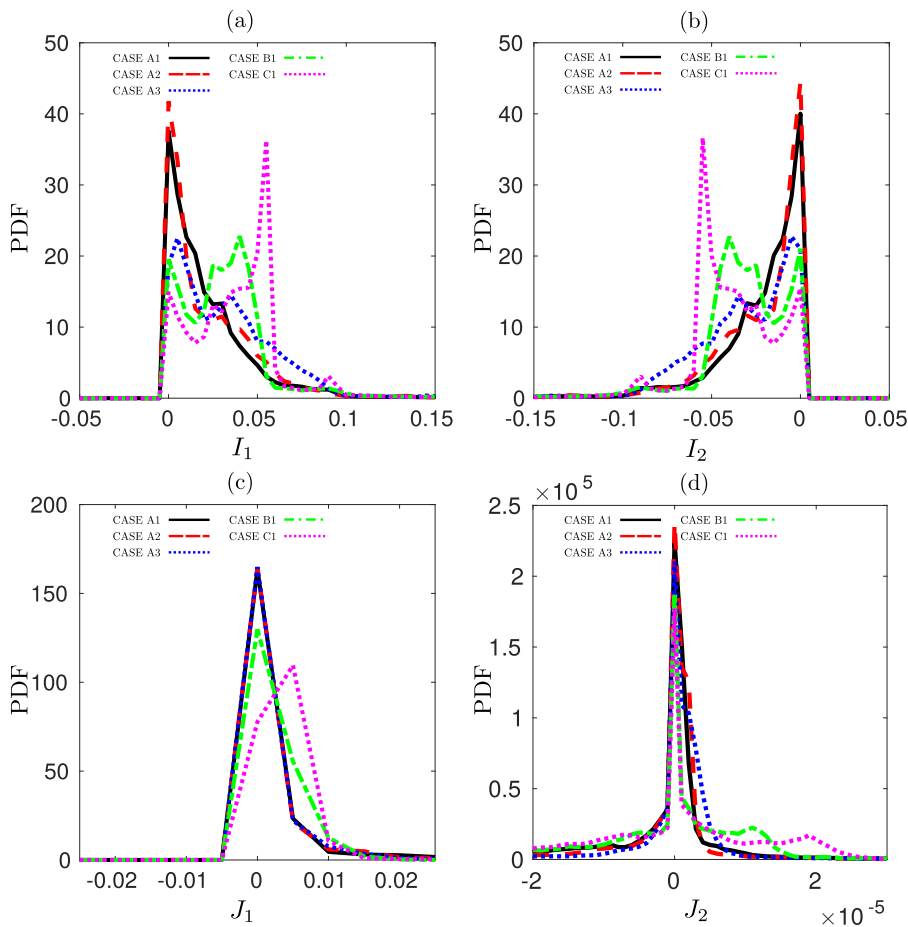
FIG. 17. PDF of basis functions (a) I_1, (b) I_2, (c) J_1, and (d) J_2 calculated from time-averaged LES data.

developed in the present study. To further investigate this matter, a statistical analysis was also performed on a selection of the basis functions [Eq. (14)] for different ranges of flow and geometry conditions. Figure 17 shows probability density functions (PDF) of basis functions I_1, I_2, J_1, and J_2 calculated from time-averaged LES data. As can be seen, the thickest lip cases with different blowing ratios (cases A1–A3) show approximately similar probability, indicating that there is no significant effect of changing the blowing ratio for a given lip thickness on the basis functions. Nonetheless, changing the lip thickness for a given blowing ratio (cases A1, B1, C1) leads to a significant alteration of the PDF profiles, particularly for I_1 and I_2, where the peaks moves from the origin. Collectively, these observations are consistent with the earlier results presented for $\overline{C}_f$ (Fig. 5) and Pr_t (Fig. 9). This suggests that the developed GEP models can be relied upon outside of the parameter space they were developed on. Again, the model trained on case A1 has been shown to significantly improve the adiabatic wall effectiveness across all the cases studied here.

F. Comparison of modeled and LES temperature field

We have so far shown the capability of the data-driven turbulence heat flux models to improve the predication of the adiabatic wall effectiveness. It is also of significance to know whether the

(a) $x/s = 25$

(b) $x/s = 50$

Legend:

- LES
- ScalarTransport on LES with $Pr_t=0.9$
- ScalarTransport on LES with $\alpha_t^{mod,1}$
- ScalarTransport on LES with $\alpha_t^{mod,2}$
- ScalarTransport on LES with $\alpha_t^{mod,3}$
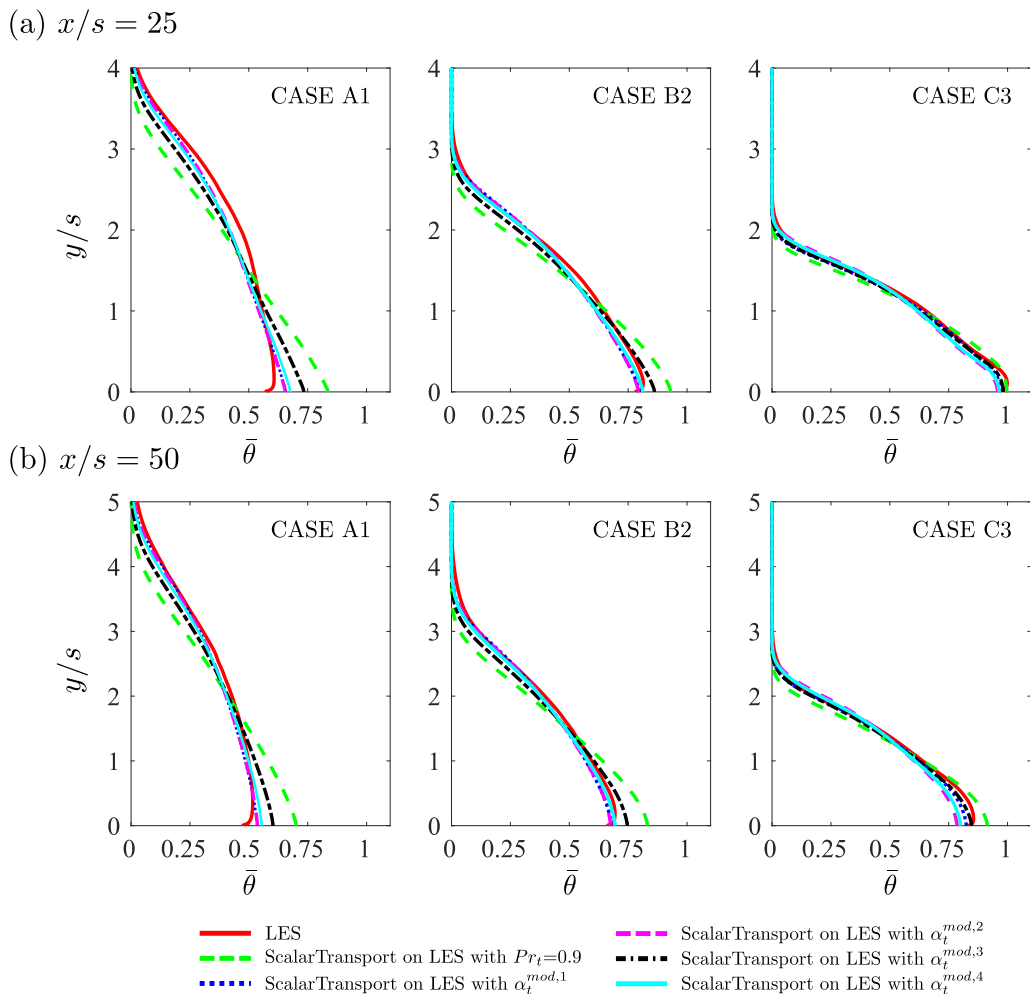- ScalarTransport on LES with $\alpha_t^{mod,4}$

FIG. 18. Comparison of the normalized temperature field obtained from different flux models.

temperature field away from the wall has consistently improved. Figure 18 therefore shows the normalized temperature profile η at two axial locations ($x/s = 25$ and $x/s = 50$) as a function of wall-normal direction (y/s) for the three cases A1, B2, and C3, using the developed models compared with the LES data and the EDM with $Pr_t = 0.9$. As can be seen, a significant improvement in the temperature field prediction away from the wall is also achieved across all the cases with different data-driven models, consistent with the improvements observed earlier for the adiabatic wall effectiveness shown in Fig. 16 and Table III. These results again highlight the capability of the developed GEP-based heat flux models in improving the prediction of the temperature field for the turbulent wall jets with coflow cases studied here.

G. Evaluation of the GEP models in a pure RANS context

We have previously shown the prediction accuracy and robustness of the GEP models when solving the scalar-transport equation [Eq. (9)] using as input the LES mean velocity field and the frozen eddy viscosity (ν_t) obtained from LES. We chose this strategy to focus on the turbulent heat
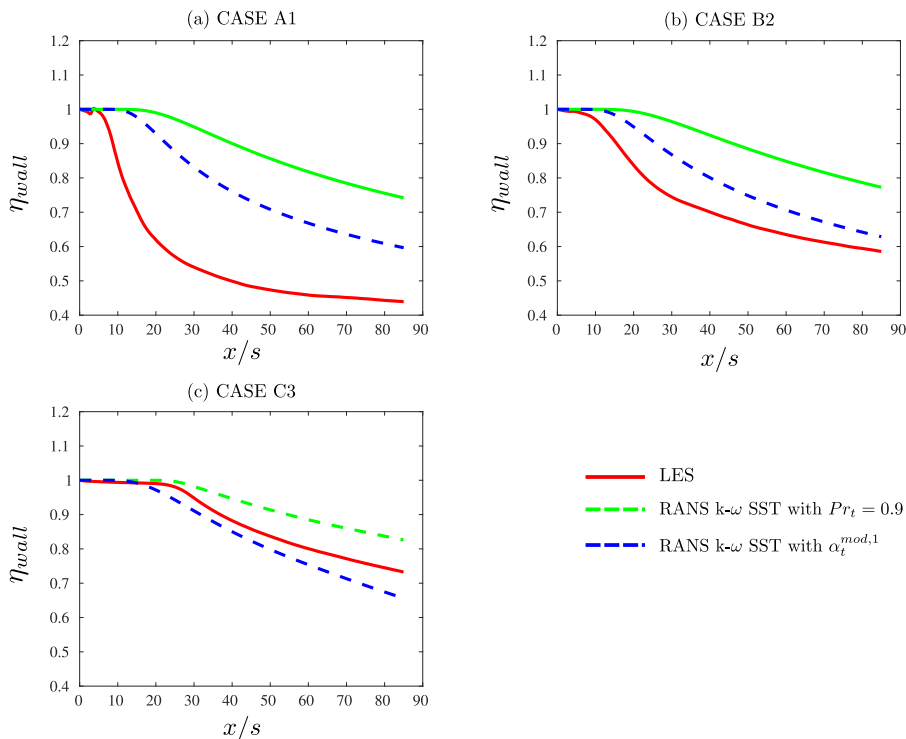
FIG. 19. Comparison of the adiabatic wall effectiveness (η_{wall}) obtained from time-averaged LES and RANS for cases A1 (a), B2 (b), and C3 (c).

flux closures only and exclude any other possible sources of error(s) such that only the contribution from the heat-flux closures (such as RANS standard eddy diffusivity model with $Pr_t = 0.9$ and also newly GEP-trained models) could be explored.

In this part, the performance of our best-performing model [i.e., $\alpha_t^{mod,1}$ Eq. (18) trained on the thickest lip wall at BR = 1.26] is evaluated in a pure RANS context for the three cases A1, B2, and C3 (diagonal of the full test matrix). The baseline 2D RANS calculations were conducted via the $k - \omega$ SST turbulence model using the standard EDM with a commonly assumed value of $Pr_t = 0.9$. The scalar-transport equation [Eq. (9)] was also solved using as input the baseline RANS velocity and eddy viscosity (ν_t) fields with $\alpha_t^{mod,1}$ Eq. (18). Figure 19 compares the adiabatic wall effectiveness between the time-averaged LES results and the results of the aforementioned RANS calculations. As can be seen, a significant improvement for the prediction of the adiabatic wall effectiveness is achieved using the present data-driven heat flux model [$\alpha_t^{mod,1}$ Eq. (18)] in a RANS context, in particular for the medium- and the thin-lip thickness cases. It is therefore understood that for a case with strong vortex shedding such as case A1 [see Fig. 19(a)], only modifying the heat flux model without improving the RANS velocity field may not give the best result and other methodologies like deriving a model for Reynolds stress are necessary. For example, a framework for data-driven turbulence modeling of flows with organized unsteadiness [49] was recently developed. The resulting closures used in URANS and PANS (partially averaged Navier-Stokes) showed significant improvement of results for a wake with strong vortex shedding. This framework may therefore give promising results when applied to the wall jets with a thick lip wall, featuring strong coherent structure in the flow field. However, combining this with developing improved heat flux models is the topic of our future research.

IV. CONCLUSIONS

In this work, data-driven models for the turbulent heat flux prediction in wall jets with coflow were developed using a gene-expression-programming-based machine-learning technique. The models were trained using invariants constructed from the strain rate and vorticity tensors and the temperature gradient vector of highly resolved large eddy simulations (LES). In total, nine LES with various lip wall thickness and blowing ratios were performed, featuring significant differences in their physical behavior. Three of these cases were selected for model development.

The GEP heat flux closures were developed by adopting gradient-diffusion hypothesis with the optimization target being a nondimensional parameter α^{gep}, which can be considered as the inverse of a *nonconstant* turbulent Prandtl number with a functional dependence on the velocity and temperature gradients. The developed closures were then tested on all cases to assess their robustness.

The RANS-based scalar-transport equation was solved using as input the LES mean velocity field with the standard eddy diffusivity model (EDM) using a commonly assumed value of $\text{Pr}_t = 0.9$. The well-known overprediction of adiabatic wall effectiveness was observed compared with the time-averaged LES results. Examination of the turbulent Prandtl number calculated from time-averaged LES data showed a significant deviation from the commonly assumed value of 0.9, with a more significant dependence on the lip wall thickness than the blowing ratio. Considering the developed heat flux models in the present study, some important points can be noted. First, the examination of the machine-learning models revealed an excellent agreement with the LES turbulent thermal diffusivity, while the EDM with $\text{Pr}_t = 0.9$ significantly underpredicted the results. Second, the developed closures were tested *a posteriori* in a RANS framework through solving the scalar transport equation using as input the LES time-averaged velocity and frozen turbulent viscosity to assess their robustness. The trained heat flux models significantly improved the prediction of adiabatic wall effectiveness not only for the cases they were trained on, but also for the entire LES cases' matrix. In particular, in terms of accuracy and robustness, the model developed on the thickest lip wall case was the best and led to an error reduction of 63–96% in the adiabatic wall effectiveness prediction across all the LES cases compared to that of the EDM with $\text{Pr}_t = 0.9$. However, the model trained on the thinnest lip wall case showed a more significant improvement in the η_{wall} profiles of this particular geometry (80–88% error reduction) compared with applying this model to the other geometries with thicker lip walls (36–56% error reduction). Third, a significant improvement in the temperature field prediction away from the wall was also achieved following the application of the data-driven models across all the cases, consistent with the improvements observed for the adiabatic wall effectiveness.

Finally, evaluation of the GEP models in a full RANS context was also conducted. The baseline RANS calculations were conducted via the $k - \omega$ SST turbulence model using the standard EDM with $\text{Pr}_t = 0.9$. The scalar-transport equation was also solved using as input the baseline RANS velocity and eddy viscosity (ν_t) fields with our best-performing GEP model (trained on the thickest lip wall case). We observed a significant improvement for the prediction of the adiabatic wall effectiveness for the medium- and the thin-lip cases, but not for the thickest lip wall case. The latter observation can be attributed to the poor steady RANS performance for a case that features strong vortex shedding and coherent structures in its flow field. This therefore implies that for a case where the effect of organized unsteadiness on the turbulence is important, only modifying the heat flux model without improving the RANS velocity field may not be sufficient and other methodologies like deriving a model for the Reynolds stress are necessary.

It is worth mentioning that the generated data-driven models capture the physical properties of the cases studied (as evidenced by their ability to significantly improve the prediction of adiabatic wall effectiveness on the training case and previously unseen, and quite different, cases) and therefore can be utilized for the prediction of the temperature field in turbulent wall jets with coflow for cases that share similar flow physics to those tested here.

---

[1] B. Launder and W. Rodi, The turbulent wall jet, Prog. Aerosp. Sci. **19**, 81 (1979).

[2] B. Launder and W. Rodi, The turbulent wall jet measurements and modeling, Annu. Rev. Fluid Mech. **15**, 429 (1983).

[3] D. Quintana, M. Amitay, A. Ortega, and I. J. Wygnanski, Heat transfer in the forced laminar wall jet, J. Heat Transfer **119**, 451 (1997).

[4] D. Ahlman, G. Brethouwer, and A. V. Johansson, Direct numerical simulation of a plane turbulent wall-jet including scalar mixing, Phys. Fluids **19**, 065102 (2007).

[5] D. Ahlman, G. Velter, G. Brethouwer, and A. V. Johansson, Direct numerical simulation of nonisothermal turbulent wall jets, Phys. Fluids **21**, 035101 (2009).

[6] I. Z. Naqvi, J. C. Tyacke, and P. G. Tucker, A numerical study of a plane wall jet with heat transfer, Int. J. Heat Fluid Flow **63**, 99 (2017).

[7] I. Z. Naqvi, J. C. Tyacke, and P. G. Tucker, Direct numerical simulation of a wall jet: Flow physics, J. Fluid Mech. **852**, 507 (2018).

[8] S. C. Kacker and J. H. Whitelaw, An Experimental investigation of the influence of slot lip thickness of the impervious wall effectiveness of the uniform density, two-dimensional wall jet, Int. J. Heat Mass Transfer **12**, 1196 (1969).

[9] G. Medic and P. A. Durbin, Unsteady effects on trailing edge cooling, J. Heat Transfer **127**, 388 (2005).

[10] J. Joo and P. A. Durbin, Simulation of turbine blade trailing edge cooling, J. Fluid Eng. **131**, 021102 (2009).

[11] T. Cebeci, A model for eddy conductivity and turbulent Prandtl number, J. Heat Transfer **95**, 227 (1973).

[12] L. Chua and R. Antonia, Turbulent Prandtl number in a circular jet, Int. J. Heat Mass Transfer **33**, 331 (1990).

[13] K. Bremhorst and L. Krebs, Eddy diffusivity based comparisons of turbulent Prandtl number for boundary layer and free jet flows with reference to fluids of very low Prandtl number, J. Heat Transfer **115**, 549 (1993).

[14] E. C. Marineau, J. A. Schetz, and R. E. Neel, Turbulent Navier-Stokes simulations of heat transfer with complex wall temperature variations, J. Thermophys. Heat Transfer **21**, 525 (2007).

[15] B. J. Daly and F. H. Harlow, Transport equations in turbulence, Phys. Fluids **13**, 2634 (1970).

[16] B. A. Younis, C. G. Speziale, and T. T. Clark, A rational model for the turbulent scalar fluxes, Proc. Royal Soc. London, Ser. A **461**, 575 (2005).

[17] J. Wissink, V. Michelassi, and W. Rodi, Heat transfer in a laminar separation bubble affected by oscillating external flow, Int. J. Heat Fluid Flow **25**, 729 (2004).

[18] M. P. Brenner, J. D. Eldredge, and J. B. Freund, Perspective on machine learning for advancing fluid mechanics, Phys. Rev. Fluids **4**, 100501 (2019).

[19] J.-L. Wu, H. Xiao, and E. Paterson, Physics-informed machine learning approach for augmenting turbulence models: A comprehensive framework, Phys. Rev. Fluids **3**, 074602 (2018).

[20] K. Duraisamy, G. Iaccarino, and H. Xiao, Turbulence modeling in the age of data, Annu. Rev. Fluid Mech. **51**, 357 (2019).

[21] R. D. Sandberg and V. Michelassi, The current state of high-fidelity simulations for main gas path turbomachinery components and their industrial impact, Flow Turbul. Combust. **102**, 797 (2019).

[22] J.-X. Wang, J.-L. Wu, and H. Xiao, Physics-informed machine learning approach for reconstructing Reynolds stress modeling discrepancies based on DNS data, Phys. Rev. Fluids **2**, 034603 (2017).

[23] J. Ling, A. Kurzawski, and J. Templeton, Reynolds averaged turbulence modelling using deep neural networks with embedded invariance, J. Fluid Mech. **807**, 155 (2016).

[24] N. Geneva and N. Zabaras, Quantifying model form uncertainty in Reynolds-averaged turbulence models with Bayesian deep neural networks, J. Comput. Phys. **383**, 125 (2019).

[25] L. Zhu, W. Zhang, J. Kou, and Y. Liu, Machine learning methods for turbulence modeling in subsonic flows around airfoils, Phys. Fluids **31**, 015105 (2019).

[26] P. A. Srinivasan, L. Guastoni, H. Azizpour, P. Schlatter, and R. Vinuesa, Predictions of turbulent shear flows using deep neural networks, Phys. Rev. Fluids **4**, 054603 (2019).

[27] E. J. Parish and K. Duraisamy, A paradigm for data-driven predictive modeling using field inversion and machine learning, J. Comput. Phys. **305**, 758 (2016).

[28] R. Matai and P. Durbin, Zonal eddy viscosity models based on machine learning, Flow Turbul. Combust. **103**, 93 (2019).

[29] J. Ray, S. Lefantzi, S. Arunajatesan, and L. Dechant, Learning an eddy viscosity model using shrinkage and bayesian calibration: A jet-in-crossflow case study, J. Risk Uncert. Eng. Syst. Part B **4**, 011001 (2018).

[30] J. Ray, L. Dechant, S. Lefantzi, J. Ling, and S. Arunajatesan, Robust Bayesian calibration of a k-ε model for compressible jet-in-crossflow simulations, AIAA J. **56**, 4893 (2018).

[31] J. Weatheritt and R. Sandberg, A novel evolutionary algorithm applied to algebraic modifications of the RANS stress-strain relationship, J. Comput. Phys. **325**, 22 (2016).

[32] C. Ferreira, Gene expression programming: A new adaptive algorithm for solving problems, Complex Syst. **13**, 87 (2001).

[33] J. Weatheritt, R. D. Sandberg, J. Ling, G. Saez, and J. Bodart, A comparative study of contrasting machine learning frameworks applied to RANS modeling of jets in crossflow, ASME Paper No. GT2017- 63403, 2017 (unpublished).

[34] J. Weatheritt, R. Pichler, R. D. Sandberg, G. M. Laskowski, and V. Michelassi, Machine learning for turbulence model development using a high fidelity HPT cascade simulation, in *Proceedings of the ASME Turbo Expo 2017: Turbomachinery Technical Conference and Exposition, Vol. 2B: Turbomachinery, Charlotte, North Carolina, USA, June 26–30, 2017* (American Society of Mechanical Engineers, 2017), p. V02BT41A015.

[35] H. Akolekar, J. Weatheritt, N. Hutchins, R. Sandberg, G. Laskowski, and V. Michelassi, Development and use of machine-learnt algebraic Reynolds stress models for enhanced prediction of wake mixing in low-pressure turbines, J. Turbomach. **141**, 041010 (2019).

[36] K. Duraisamy and P. Durbin, Transition modeling using data driven approaches, in *Proceedings of the CTR Summer Program* (2014), p. 427.

[37] Z. J. Zhang and K. Duraisamy, Machine learning methods for data-driven turbulence modeling, in *22nd AIAA Computational Fluid Dynamics Conference* (AIAA, New York, 2015), p. 2460.

[38] P. M. Milani, J. Ling, G. Saez-Mischlich, J. Bodart, and J. K. Eaton, A machine learning approach for determining the turbulent diffusivity in film cooling flows, J. Turbomach. **140**, 021006 (2018).

[39] P. M. Milani, J. Ling, and J. K. Eaton, Physical interpretation of machine learning models applied to film cooling flows, J. Turbomach. **141**, 011004 (2019).

[40] R. Sandberg, R. Tan, J. Weatheritt, A. Ooi, A. Haghiri, V. Michelassi, and G. Laskowski, Applying machine learnt explicit algebraic stress and scalar flux models to a fundamental trailing edge slot, J. Turbomach. **140**, 101008 (2018).

[41] R. Sandberg, Compressible-flow DNS with application to airfoil noise, Flow Turbul. Combust. **95**, 211 (2015).

[42] R. D. Sandberg, Direct numerical simulations for flow and noise studies, Proc. Eng. **61**, 356 (2013).

[43] B. Vreman, B. Geurts, and H. Kuerten, Subgrid-modelling in LES of compressible flow, Appl. Sci. Res. **54**, 191 (1995).

[44] F. Ducros, F. Nicoud, and T. Poinsot, Wall-adapting local eddy-viscosity models for simulations in complex geometries, *Conference on Numerical Methods in Fluid Dynamics* (Oxford University Computing Laboratory, Oxford, 1998) pp. 293-299.

[45] F. Nicoud and F. Ducros, Subgrid-scale stress modeling based on the square of the velocity gradient tensor, Flow Turbul. Combust. **62**, 183 (1999).

[46] R. D. Sandberg and N. D. Sandham, Nonreflecting zonal characteristic boundary condition for direct numerical simulation of aerodynamic sound, AIAA J. **44**, 402 (2006).

[47] G. Fabris, Conditional sampling study of the turbulent wake of a cylinder. Part 1, J. Fluid Mech. **94**, 673 (1979).

[48] J. R. Koza, Genetic programming as a means for programming computers by natural selection, Stat. Comput. **4**, 87 (1994).

[49] C. Lav, R. D. Sandberg, and J. Philip, A framework to develop data-driven turbulence models for flows with organised unsteadiness, J. Comput. Phys. **383**, 148 (2019).